Dalton Transactions

ROYAL SOCIETY OF CHEMISTRY

PAPER

View Article Online
View Journal | View Issue

Cite this: *Dalton Trans.*, 2023, **52**, 12755

Crystal water intercalated interlayer expanded MoS_2 nanosheets as a cathode for efficient zinc-ion storage†

Muruganandham Hariram,[a] Manoj Kumar,[a] Kamlendra Awasthi,[a] Debasish Sarkar*[a] and Prashanth W. Menezes *[b,c]

Zinc-ion batteries (ZIBs) have attracted tremendous interest from the scientific community in recent years due to their extreme safety, cost-effectiveness, environmental benignity and the unique properties of the Zn anode. However, more suitable cathode materials are needed to achieve their potential widespread applications. MoS_2, a 2D layered material with fascinating properties, could also serve as a cathode in ZIBs but is rarely studied due to its limited interlayer spacing, poor ionic/electronic conductivity and hydrophobicity. In this work, we report a facile hydrothermal method for synthesizing crystal water-intercalated MoS_2 nanosheets and their application in efficient Zn-ion storage. Morphological characterization reveals the average thickness of the nanosheets to be 15.2 nm. With a large interlayer spacing (0.79 nm), high 1T content (49.7%) and high defects, $MoS_2{\cdot}nH_2O$ achieves a high discharge capacity of 197 mA h g^{-1} at 0.1 A g^{-1} in an aqueous 2 M $ZnSO_4$ electrolyte. Moreover, it exhibits modest cyclic stability with 55% capacity retention after 1000 charge/discharge cycles. Furthermore, we evaluated the charge storage kinetics of crystal water-intercalated MoS_2 nanosheets and realized that the electrochemical reaction is diffusion dominated with a diffusion coefficient of 10^{-10} to 10^{-13} cm^2 s^{-1} in a 0.3 to 1.3 V potential window. This simple and cost-effective strategy for improving the performance of ZIBs by crystal water intercalation in 2D cathode materials will pave the way for their commercial-level grid-scale applications.

Received 27th June 2023,
Accepted 9th August 2023

DOI: 10.1039/d3dt02001k

rsc.li/dalton

1. Introduction

The increasing energy crises and environmental concerns are the great challenges of the current era, which have led to the paradigm shift towards renewable energy sources. In recent decades, rechargeable batteries have played a significant role in this paradigm shift by acting as an efficient storage medium for intermittent energy sources. In particular, lithium-ion batteries (LIBs) have entirely dominated the energy storage sector because of their high energy density and long cycle life. However, they suffer from numerous factors, including scarcity of lithium resources, high cost, safety issues and flammability of organic electrolytes, which impede their next-generation stationary grid-scale applications.[1] Therefore, developing a high-performance energy storage system with low-cost, safe and environmentally benign materials is of foremost importance in the current scenario. In this regard, aqueous zinc-ion batteries (ZIBs) received significant attention due to their superior safety, abundance, good chemical stability, cost-effectiveness (~$65 per kW per h *vs.* ~$300 per kW per h of LIBs), high ionic conductivity (0.1–6 S cm^{-1} *vs.* 10^{-3}–10^{-2} S cm^{-1} of LIBs), high theoretical capacity (5855 mA h cm^{-3} and 820 mA h g^{-1}), low redox potential of Zn/Zn^{2+} (−0.763 V *vs.* standard hydrogen electrode) and eco-friendliness.[2] Nevertheless, ZIBs are far from reaching the performance of LIBs because of their sluggish diffusion kinetics arising from divalent Zn^{2+} ions and zinc dendrite formation at the anode. More importantly, insertion/extraction of Zn^{2+} and H^+ ions by insertion and conversion reactions generally lead to volume expansion, lattice distortion and phase transition of the cathode material, which results in their sudden death.[3] Therefore, finding a suitable cathode material for ZIBs is essential. Currently, vanadium and manganese-based oxides, Prussian blue analogues, transition metal dichalcogenides (TMDs), and organic materials are the commonly used cathode materials.

Layered TMDs, which constitute one metal-atom layer sandwiched between a pair of chalcogen-atom layers through weak van der Waals interaction, are highly beneficial for storing

[a]*Department of Physics, Malaviya National Institute of Technology Jaipur, Rajasthan 302017, India. E-mail: deb.sarkar1985@gmail.com, debasish.phy@mnit.ac.in*
[b]*Material Chemistry Group for Thin Film Catalysis – CatLab, Helmholtz-Zentrum Berlin für Materialien und Energie, Albert-Einstein-Str. 15, 12489 Berlin, Germany. E-mail: prashanth.menezes@helmholtz-berlin.de*
[c]*Department of Chemistry, Technical University of Berlin, Straße des 17 Juni 135. Sekr. C2, 10623 Berlin, Germany. E-mail: prashanth.menezes@mailbox.tu-berlin.de*
† Electronic supplementary information (ESI) available. See DOI: https://doi.org/10.1039/d3dt02001k

guest ions through insertion/extraction.[4] Their layered configuration can accommodate the volume variation during the insertion/extraction of ions and facilitate mass ion transportation. In particular, molybdenum disulfide (MoS_2), a well-known 2D layered material having an interlayer spacing of 6.15 Å, is a promising host material for various energy storage systems, including LIBs, sodium-ion batteries (NIBs) and supercapacitors.[5] Moreover, MoS_2 also possesses high theoretical capacity, low cost, high surface areas and multiple phase configurations (metallic 1T and semiconducting 2H). However, in ZIBs, MoS_2 exhibits poor performance in terms of both capacity and cyclic stability due to the following reasons. Firstly, Zn^{2+} ions with a large hydrated ion size (0.404–0.43 nm) have to overcome the high desolvation energy barrier during insertion into the relatively narrow interlayers of MoS_2. Secondly, strong electrostatic interaction between Zn^{2+} and anions hinders its diffusion kinetics. Moreover, the poor ionic/electronic conductivity and low hydrophilicity of MoS_2 have also been a severe hindrance to its performance.[6,7]

To surmount the abovementioned problems, researchers have adopted various modification strategies such as interlayer engineering for expanding lattices of MoS_2, defect engineering by introducing S and Mo vacancies, phase engineering by controlling the 1T/2H content of MoS_2 and hybridization with other conductive materials.[4] By expanding the interlayer spacing of MoS_2, one can facilitate the effective insertion of Zn^{2+} ions and reduce ion diffusion resistance without lattice breathing.[8] For interlayer expansion, researchers pre-intercalated the MoS_2 lattice with guest species such as NH_3, oxygen, crystal water, metal ions and carbon nanostructures.[9–12] For instance, Yao *et al.*[13] reported the cetyltrimethylammonium bromide (CTAB)-intercalated MoS_2 superstructure, which significantly expands the interlayer spacing to 1.0 nm. CTAB intercalation endows structural stability to MoS_2 by acting as a buffer layer to alleviate volume expansion during Zn^{2+} insertion/extraction, which results in high specific capacity (181 mA h g^{-1} at 0.1 A g^{-1}) and ultralong cyclic stability (~92.8% after 2100 cycles). Similarly, Liu *et al.*[14] showed monolayer water-inserted 1T-MoS_2 with an interlayer spacing of 0.91 nm and obtained the maximum specific capacity of 164.1 mA h g^{-1} at 0.1 A g^{-1}, which is 6–8 times that of pristine 2H-MoS_2. Recently, MWCNTs@amorphous carbon@MoS_2 (MWCNTs = multi-walled carbon nanotubes) with a large interlayer spacing of 0.88 nm was prepared by Niu and co-workers, in which a high specific capacity of 181 mA h g^{-1} at 0.1 A g^{-1} with a rate capability of 110 mA h g^{-1} at 12 A g^{-1} was observed.[15] Therefore, optimizing MoS_2 with enlarged interlayer spacing and better structural stability by pre-intercalation with guest species is an effective strategy for alleviating Zn-ion storage.

In this work, we have demonstrated a facile, scalable and low-cost hydrothermal route for synthesizing crystal water-intercalated MoS_2 nanosheets ($MoS_2{\cdot}nH_2O$) using sodium molybdate and thiourea as the Mo and S sources, respectively. The as-synthesized MoS_2 nanosheets are defective, having a large interlayer spacing of 0.79 nm and a high degree of the 1T-phase component. Benefitting from their structural and morphological traits, the hydrated nanosheets exhibit a high reversible specific capacity of 197 mA h g^{-1} at 0.1 A g^{-1} with a good rate performance and cycle life as a ZIB cathode.

2. Experimental section

2.1. Synthesis of $MoS_2{\cdot}nH_2O$ nanosheets

Crystal water-intercalated MoS_2 was prepared by a facile one-step hydrothermal reaction. 3.327 g of sodium molybdate (Sigma Aldrich) and 6.84 g of thiourea (Loba Chemie) were mixed with 72 mL of de-ionized water (DI) by constant stirring at room temperature for 1 h. After that, the reaction mixture was transferred into a 100 mL Teflon-lined autoclave and kept at 200 °C for 24 h. After cooling to room temperature, the obtained black-coloured precipitate was collected and centrifuged with DI and ethanol several times until the pH was neutralized. The final product was obtained by vacuum drying the sample at 80 °C overnight. The possible synthesis reaction mechanism is mentioned below:

$$CS(NH_2)_2 + 2H_2O \rightarrow 2NH_3 + CO_2 + H_2S \quad (1)$$

$$4Na_2MoO_4 + 15CS(NH_2)_2 + 6H_2O \rightarrow 4MoS_2 + Na_2SO_4 + 6NaSCN + 24NH_3 + 9CO_2 \quad (2)$$

2.2. Material characterization techniques

The crystalline properties of the as-synthesized MoS_2 were studied through the X-ray diffraction technique (XRD, Panalytical X-pert Pro diffractometer) with Cu-Kα irradiation (λ = 1.5406 Å) with 2θ values ranging from 5° to 50°. Raman spectroscopy analysis was carried out using an Airix Corp. STR 500 Raman spectrophotometer using a 532 nm laser with a power of 15 mW. Furthermore, the thermal profile of the material was analysed using a thermogravimetric analyser (TGA, STA 6000 PerkinElmer) under an oxygen atmosphere from room temperature to 700 °C at a heating rate of 10 °C min^{-1}. The elemental composition and electronic configuration of the sample were studied through X-ray photoelectron spectroscopy (XPS, ESCA+ Omicron Nano Technology). The morphology of the as-synthesized material was studied through field-emission scanning electron microscopy (FESEM, Quanta 250 FEG) along with energy dispersive X-ray spectroscopy (EDS), transmission electron microscopy (TEM, ThermoFisher, Talos F200S G2) and high-resolution TEM (HRTEM) with electron energy loss spectroscopy (EELS). The Fourier-transform infrared spectroscopy (FTIR) technique was performed using an FTIR spectrometer (PerkinElmer) in the range of 4000–400 cm^{-1} in KBr mode. The specific surface area of the samples was measured using a Brunauer–Emmett–Teller (BET) surface area analyser (Nova Touch LX2 gas sorption analyser, Quantachrome Instruments), while the pore-size distribution and pore volume were calculated using a Barrett–Joyner–Halenda (BJH) model.

2.3. Fabrication of electrodes and cell assembly

To fabricate the cathode, MoS_2, acetylene black (Alfa Aesar, ~99%) and polyvinylidene fluoride (PVDF, Sigma-Aldrich) were mixed and ground well in an 8 : 1 : 1 ratio. A few drops of *N*-methyl-2-pyrrolidone (Alfa Aesar, ~99%) were added to make a homogeneous slurry. Furthermore, the slurry was coated on stainless steel electrodes using doctor blades and dried at 80 °C overnight. Zinc foil was used as the anode. The cell was assembled in a pouch by sandwiching Whatman filter paper (separator) between the electrodes, and 2–3 drops of 2 M $ZnSO_4$ (electrolyte) were added. The cell was kept at rest for 3 h before starting measurements.

2.4. Electrochemical characterization techniques

The assembled ZIBs were studied through cyclic voltammetry (CV) at different scan rates (0.1 to 5 mV s^{-1}) and galvanostatic charge–discharge (GCD) at different current densities (0.1 to 2 A g^{-1}). Electrochemical impedance spectroscopy (EIS) was performed between 100 kHz and 10 mHz with a perturbation voltage of 5 mV at an open circuit potential. The cycling performance of the as-fabricated ZIBs was studied for 1000 charge/discharge cycles at 2 A g^{-1}. Moreover, to understand the kinetics of ZIBs, a galvanostatic intermittent titration test (GITT) was also performed by charging and discharging the cell at 0.1 A g^{-1} for 8 min and relaxing for 32 min to achieve equilibrium. A CHI760E electrochemical workstation was used for CV and EIS measurements, while the Neware battery testing system (BTS4000-5V20 mA) was used for galvanostatic charge/discharge (GCD), cycling and GITT measurements. The details about the calculations are given in the ESI.†

3. Results and discussion

3.1. Material characterization

The facile and scalable technique for preparing crystal water-intercalated interlayer expanded MoS_2 nanosheets is reported in this work. The reaction mechanism for the formation of MoS_2 can be represented using eqn (1) and (2). It involves the hydrolysis of $CS(NH_2)_2$ to form H_2S and the reduction of Mo(VI) into Mo(IV), which results in the formation of MoS_2. The other chemical species (mainly ammonium ions, oxygen, and hydrated Na^+ ions) formed during hydrothermal reactions may get trapped in the interlayers of MoS_2. This assists the formation of chemical bonding between oxygen from water molecules and MoS_2, resulting in the enlarged interlayer spacing.[16] The morphological characterization was performed by FESEM, TEM and HRTEM analyses. Fig. 1(a and b) show the FESEM images of the as-synthesized $MoS_2{\cdot}nH_2O$ nanosheets having 2D sheet-like morphology. However, some deformed structures are also present, which may arise from the agglomeration of nanosheets during the long reaction time. Fig. 1(c) shows the thickness distribution of the MoS_2 nanosheets. The size and shape of the as-synthesized nanosheets are almost uniform, with an average thickness of 15.2 nm. The EDX pattern of the as-synthesized MoS_2 is shown in Fig. S1,† which confirms the existence of Mo, S and O in the sample. From EDX, the atomic % of S (28.9%) was found to be almost twice that of Mo (15.2%), confirming the formation of MoS_2. The TEM image (Fig. 1d) also confirms the petal-like morphology of MoS_2 with a dimension of 190 × 250 nm. Fig. 1(e) shows the HRTEM image of MoS_2 in which the interlayer spacing of the (002) plane was calculated to be 0.78 nm, which is higher than the standard interlayer spacing of MoS_2, suggesting the intercalation of crystal water. It also shows the presence of defects in the lattice planes. The interlayer expanded nanostructure with lattice defects will benefit the electrochemical performance of MoS_2 nanostructures since it can effectively decrease the ion diffusion resistance and provide more electrochemically active sites.[17,18] The SAED pattern in Fig. 1(f) exhibits circular fringes, which suggests the polycrystalline nature of the sample with the (002), (004), (100), (105) and (112) planes of MoS_2. Fig. 1(g–i) show the high-angle annular dark field scanning transmission electron microscopy (HAADF-STEM) image and EELS mapping of the MoS_2 nanosheets, which confirms the homogeneous distribution of Mo and S in the sample.

The physicochemical properties of the as-synthesized MoS_2 nanosheets were studied through powder XRD. Fig. 2(a) shows the XRD pattern of MoS_2 in which the broad diffraction peak centered at $2\theta = 11.09°$ corresponds to the diffraction from the (002) plane of 1T MoS_2. The peak shift from 14.125° to 11.09° implies an enlarged interlayer spacing of 0.79 nm, which is in accordance with the HRTEM results. This expansion in interlayer spacing is due to the intercalation of crystal water during the hydrothermal reaction. The remaining peaks at 28.81° and 32.87° correspond to the (004) and (100) planes of 2H-MoS_2 (JCPDS: 01-075-1539). Therefore, the as-synthesized sample has the mixed phases of 1T and 2H MoS_2. Moreover, the absence of higher-order diffraction peaks reveals the poor crystallinity of the sample material. Fig. 2(b) shows the Raman spectra of the sample in which two peaks were observed at 384 cm^{-1} and 412 cm^{-1}. These peaks are associated with in-plane E^1_{2g} vibrations and vertical-plane A_{1g} vibrations, respectively.[19] This further validates the formation of MoS_2. The thermogravimetric (TGA) spectrum of MoS_2 (Fig. 2c) shows three-step weight loss. The initial weight loss of 4.5% below 250 °C is due to the desorption of surface water from the sample. The second weight loss of 4.7% observed between 250 and 500 °C represents the loss of crystal water.[20] Furthermore, the huge weight loss above 500 °C is due to the oxidation of MoS_2 to form MoO_3. From the TGA curve, the molar ratio of MoS_2 and crystal water was estimated to be 1 : 0.51. To further confirm the existence of crystal water in the MoS_2 lattice, XPS was performed, and the results are depicted in Fig. 2(d–f). The survey spectrum in Fig. S2† confirms the presence of Mo, S and O in the sample. The high-resolution spectrum of Mo 3d (Fig. 2d) shows three main peaks at binding energies of 228.7 eV, 231.98 eV and 226.16 eV corresponding to Mo $3d_{5/2}$, Mo $3d_{3/2}$ and S 2s, respectively.[8] The deconvoluted Mo 3d spectra reveal the presence of doublet peaks with an energy difference of about 1 eV which can be ascribed to the presence of the mixed 1T/2H phases of MoS_2. Due to the difference in the sym-

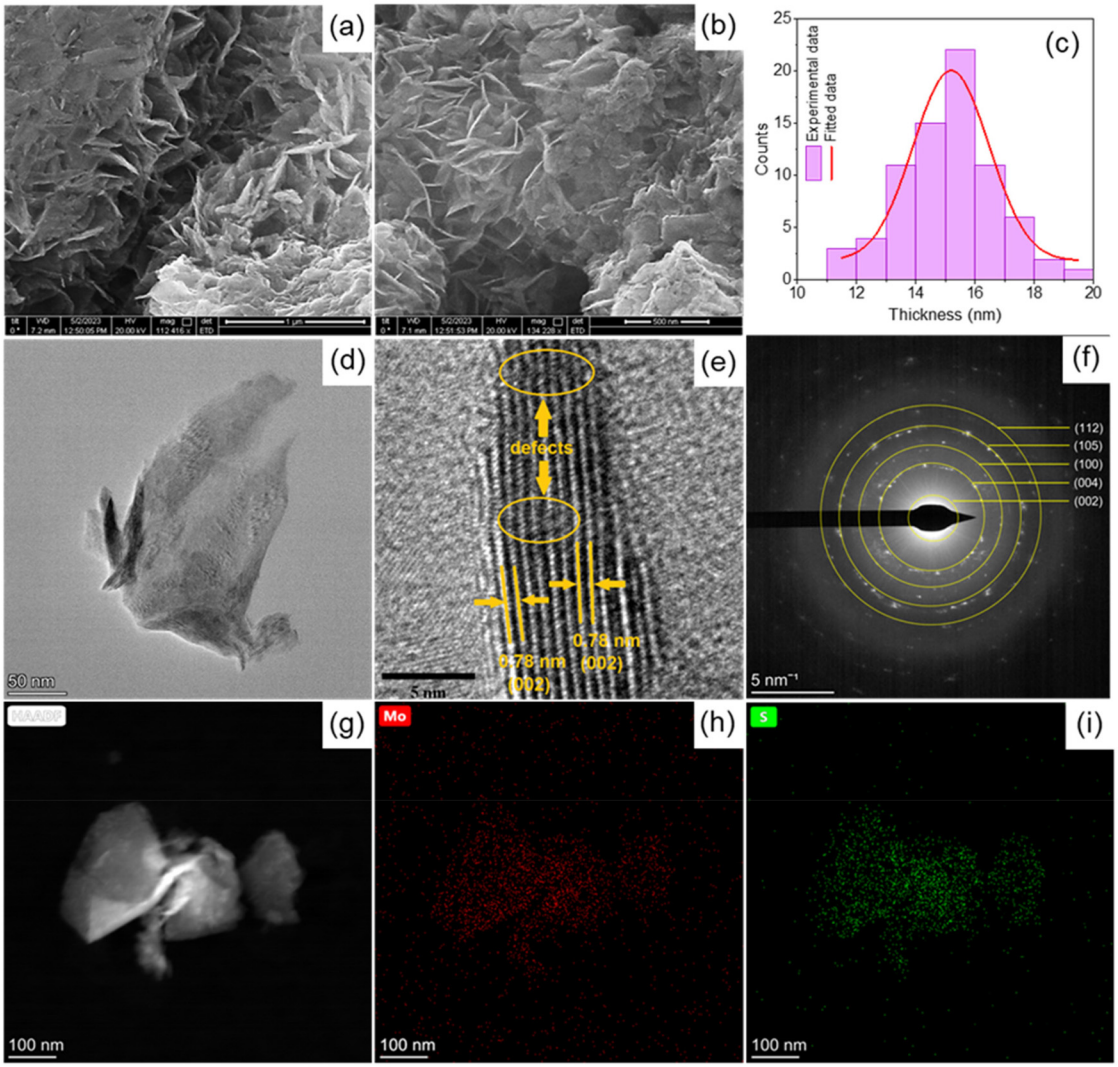

Fig. 1 (a and b) FESEM images of the synthesized MoS_2 nanosheets and their (c) thickness distribution graph. (d) TEM, (e) HRTEM, and (f) SAED pattern of the MoS_2 nanosheets, (g) high-angle annular dark field scanning transmission electron microscopy (HAADF-STEM) image, and (h and i) EELS mapping of different constituent elements of the as-synthesized MoS_2 nanosheets.

metry of 1T and 2H MoS_2 phases, there is a difference in their binding energies, leading to the parallel shift of peaks. From the XPS analyses, the amount of the 1T phase in the nanosheets was calculated to be 49.7%. Similarly, the deconvoluted S 2p spectrum as shown in Fig. 2e also confirms the existence of the 1T phase. Furthermore, the deconvoluted O 1s spectrum in Fig. 2f shows three peaks at 530.5, 531.2 and 533.3 eV binding energies, corresponding to the Mo–O, Mo–O–H and H–O–H bonding.[21] The peak at 533.3 eV confirms the presence of interlayer water, while those at 530.5 eV and 531.2 eV correspond to the lattice oxygen and surface-adsorbed oxygen species in MoS_2. This interlayer water is expected to provide a shielding effect to the Zn^{2+} ions during their intercalation/extraction with the metallic host material. FTIR analysis was performed to further validate the existence of interlayer water, and the resultant spectra are depicted in Fig. S3.† The absorption bands at 432 cm^{-1}, 532 cm^{-1}, 661 cm^{-1}, 1216 cm^{-1} and 1366 cm^{-1} correspond to the stretching vibrations of Mo–S bands, which confirms the formation of MoS_2.[22,23] The intense absorption peak at 1738 cm^{-1} is attributed to the bending vibrations of OH groups while 3713 cm^{-1} and 3779 cm^{-1} are the characteristic bands of O–H stretching vibrations.[24] These strong absorption peaks of O–H groups suggest the presence of crystal water in the as-prepared MoS_2 nanosheets. Moreover, Brunauer–Emmett–Teller (BET) and Barrett–Joyner–Halenda (BJH) analyses were also performed to find out the surface area and pore-size distribution of the sample. The N_2 adsorption–desorption isotherm (Fig. S4a†) shows a type-II isotherm with an H_3 type hysteresis loop, according to IUPAC classifications.[25] This further implies that the as-synthesized MoS_2 has aggregates of plate-like particles with slit-shaped pores.[25] The specific surface area of the MoS_2 nanosheets was calculated to be 25.843 $m^2\ g^{-1}$. Moreover, the BJH pore size distribution plot (Fig. S4b†) shows that the

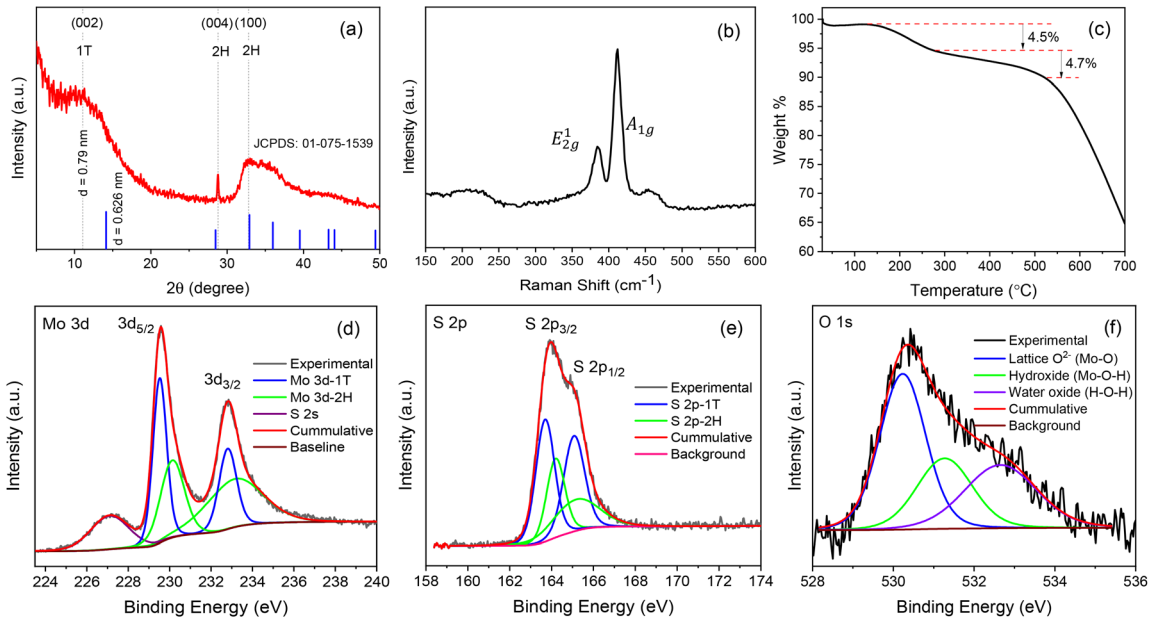

Fig. 2 (a) XRD, (b) Raman, and (c) TGA analyses of $MoS_2{\cdot}nH_2O$ nanosheets; deconvoluted high-resolution XPS spectra of (d) Mo 3d, (e) S 2p and (f) O 1s.

majority of the pores have a size in the range of 0.2–2 nm with the mean pore radius and pore volume as 1.7 nm and 0.036 cm^3 g^{-1}, respectively. With such enlarged interlayer spacing, intercalated water and high 1T phase content, the as-synthesized MoS_2 sample is expected to exhibit elevated electrochemical performance.[24] To confirm that, we have explored the as-synthesized MoS_2 nanosheets as the cathode material for zinc-ion batteries (ZIBs).

3.2. Electrochemical characterization

The aqueous ZIB was fabricated using Zn foil as the anode, $MoS_2{\cdot}nH_2O$ as the cathode, and 2 M $ZnSO_4$ as the electrolyte. Initially, to confirm the working potential of MoS_2, GCD was tested from 0.3 to 1.3, 1.4 and 1.5 V (Fig. S5†). Severe loss in the rate capability of MoS_2 shows the optimum voltage window to be 0.3 to 1.3 V. This loss in rate capability at the large potential window is due to the irreversible intercalation of Zn^{2+} ions. Furthermore, to confirm the optimal mass loading of the cathode, MoS_2 electrodes with different mass loadings were tested, and the results are depicted in Fig. 3(a). The decrease in the specific capacity at a high mass loading is due to the increase in the thickness of the electrode, which affects the penetration of the electrolyte ions into the bulk of the electrode material and hence, increases the internal resistance of the electrode.[26]

The maximum specific capacity was obtained for the cathode with 1.68 mg, which was taken for further characterization. Cyclic voltammetry (CV) was performed at the scan rates of 0.1 to 2 mV s^{-1} which is depicted in Fig. 3(b). Two redox humps were observed at around 1.1 V (anodic) and 0.5 V (cathodic), which are the typical oxidation and reduction peaks of MoS_2.[27] From the data, the specific capacity was calculated to be 180 mA h g^{-1} at 0.1 mV s^{-1} (Fig. 3c). It also showed good retention at higher scan rates with 80 mA h g^{-1} at 5 mV s^{-1}. Fig. 3(d) shows their GCD plots at different current densities ranging from 0.1 to 2 A g^{-1}. The maximum discharge-specific capacity of 197 mA h g^{-1} was observed at 0.1 A g^{-1}, which is higher than most of the reported values of MoS_2 as a ZIB cathode as summarized in Table S1.† Fig. 3(e) shows the variation of specific capacity with current densities for 50 cycles. For the 5th cycle, the specific discharge capacities were 197, 165.6, 151.1, 141.39, 137.03, 116.4, 98.18 and 83.07 mA h g^{-1} for 0.1, 0.2, 0.3, 0.4, 0.5, 1, 1.5, 2 A g^{-1}, respectively. More importantly, when the current density was reversed back to 0.1 A g^{-1}, a discharge capacity of 167 mA h g^{-1} was obtained with a recovery rate of 85%. This implies the good reversibility of the material and fast reaction kinetics. The increased interlayer spacing by the crystal water eases the intercalation/extraction process, which results in good specific capacity and reversibility. The possible electrochemical reaction between the $MoS_2{\cdot}nH_2O$ cathode and Zn anode is summarized below:

$$\text{Cathode}: \ xZn^{2+} + 2xe^- + MoS_2 \leftrightarrow Zn_xMoS_2 \quad (3)$$

$$\text{Anode}: \ xZn^{2+} + 2xe^- \leftrightarrow xZn \quad (4)$$

The amount of Zn^{2+} in the lattice of MoS_2 (xZn^{2+}), calculated from Faraday's equation, was found to be 0.59 at 0.1 A g^{-1}. Therefore, while charging, 0.59 Zn^{2+} ions per formula unit can intercalate into the MoS_2 layers to form $Zn_{0.59}MoS_2$. The discharge process takes place with the removal of 0.59e$^-$ to form 0.59 Zn. Electrochemical impedance spectroscopy (EIS) (Fig. 3f) was performed between 10 mHz and 100 kHz with a perturbation AC voltage of 5 mV. From that, the equivalent

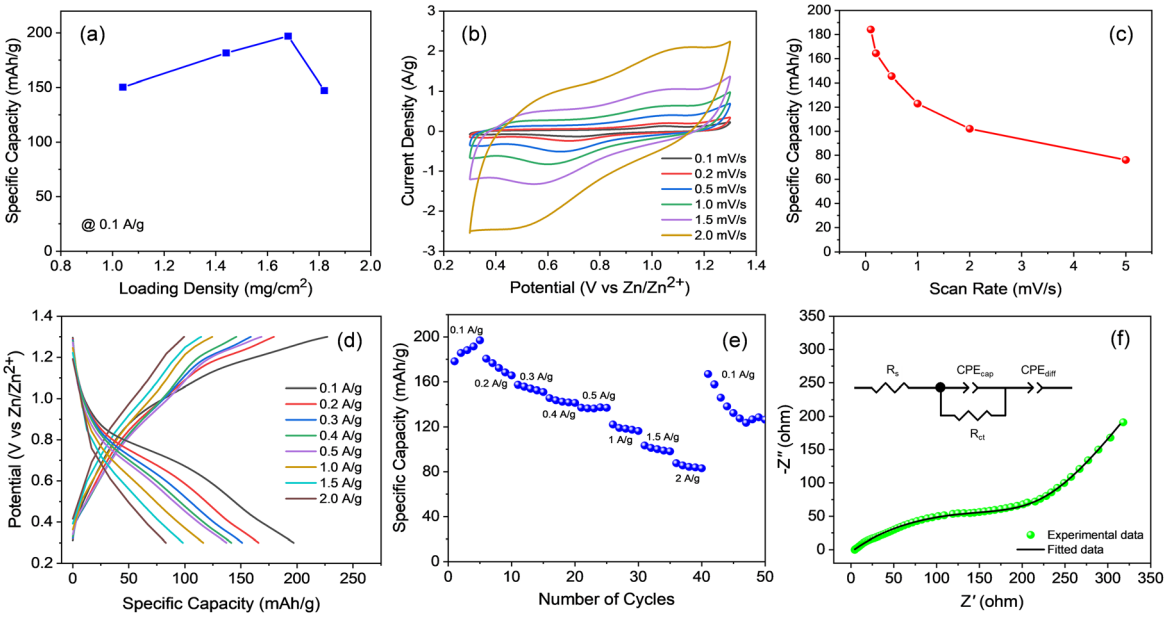

Fig. 3 (a) Comparison of specific capacity of MoS_2 at different loading densities, (b) CV at different scan rates, (c) specific capacity obtained at different scan rates, (d) GCD at different current densities, (e) specific capacity obtained at different current densities for 50 cycles and its (f) Nyquist plot (inset: equivalent circuit model).

series resistance (R_s) and charge-transfer resistance were calculated to be 3.72 and 236.4 ohm, respectively. Furthermore, Fig. S6† shows the cycling performance of the as-fabricated ZIBs at 2 A g^{-1}. An initial capacity loss of 40% was observed during the first 100 cycles, which might be due to the poor accessibility of Zn^{2+} ions to the bulk region of the electrode material. However, after 100 cycles, the discharge capacity gets almost saturated and retained an overall retention of 55% after 1000 cycles.

To evaluate the charge storage mechanism of the as-synthesized MoS_2 cathode, the capacitive and diffusive parts of the electrochemical reaction were segregated using eqn (S1).† Generally, b-values range between 0.5 and 1, in which b = 0.5 signifies the diffusion-controlled electrochemical process and b = 1 denotes the capacitive-controlled electrochemical process.[28] Using the oxidation and reduction peak current values obtained from CV, b values were calculated to be 0.74 and 0.71, respectively (Fig. 4a). This denotes that the fabricated ZIBs show both capacitive and diffusive contributions. In order to find the ratio of these contributions, capacitive and diffusive currents were calculated according to eqn (S2).† Fig. 4(b) shows the percentage of capacitive contribution at 0.1 mV s^{-1}, which was calculated to be 32%. This signifies that the majority of the charge storage capacity (68%) was contributed by a diffusion-controlled intercalation reaction, confirming their battery-type charge storage behaviour. Likewise, capacitive and diffusive capacities for different scan rates are depicted in Fig. 4(c). The ratio of capacitive contribution increases steadily with the increase in scan rates which can be explained by the fact that the diffusion-controlled process is much slower than the capacitive-controlled process.[29] To further study the diffusion kinetics of MoS_2, a galvanostatic intermittent titration technique (GITT) was performed (Fig. 4d). The GITT is the widely accepted method for calculating ion diffusivity and electrode kinetics.[30] From the GITT, the Zn^{2+} diffusion coefficient (D_{Zn}) was calculated according to the eqn (S3)† and was found to be in the range of 10^{-10} to 10^{-13} cm^2 s^{-1} at the range of 0.3 to 1.3 V. The value of D_{Zn} is relatively higher than the reported values of MoS_2, which implies that the as-synthesized MoS_2 nanosheets exhibit faster Zn^{2+} migration.[14,31] This can be associated with the enlarged interlayer spacing of MoS_2 effectively weakening the diffusion barrier of Zn^{2+} ions and hence, improving its hydrophilicity.[14,32] Moreover, Zn^{2+} diffusion coefficient of the discharge state was almost stable, highlighting the good structural stability of the as-synthesized MoS_2 in different insertion states.[33] The diffusion coefficient can also be calculated by EIS analysis using eqn (S4).† From Fig. 4(e), the Warburg factor (σ) was calculated to be 16.71. On substituting σ, D_{Zn} was calculated to be 1.61×10^{-13} cm^2 s^{-1}, which is in accordance with the GITT results. Based on the above results, it can be argued that the crystal water intercalation is assisting the electrochemical performance of MoS_2 as the ZIB cathode in the following ways: (i) crystal water intercalation expands the interlayer spacing of MoS_2, which significantly reduces its diffusion barrier and mitigates the volume expansion during intercalation/extraction of Zn^{2+} ions,[34] (ii) the presence of crystal water reduces the electrostatic repulsion between positive Zn^{2+} ions and anions of the host material, which results in better diffusion kinetics,[33] and (iii) crystal water can improve the hydrophilicity of MoS_2 by acting as a lubricant, which further accelerates the ion transportation.[17,35]

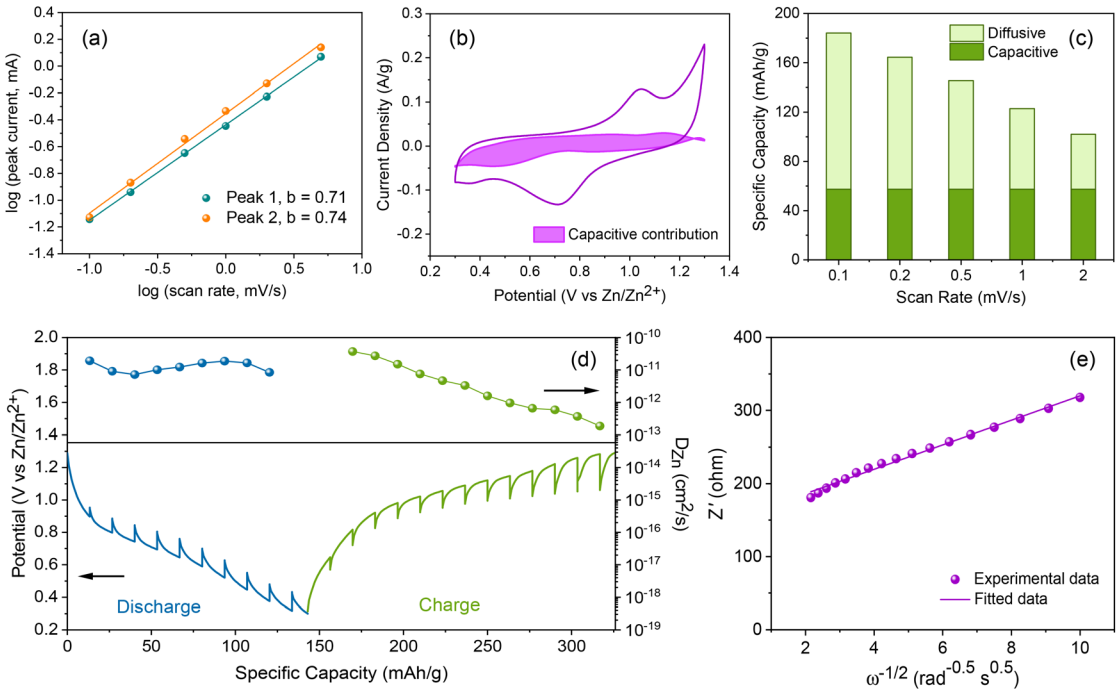

Fig. 4 (a) Log (peak current) *vs.* log (scan rate) plot of MoS_2 calculated from CV, (b) capacitive and diffusive charge segregation calculated at 0.1 mV s^{-1}, (c) capacitive and diffusive contributions towards total charge stored in MoS_2 at different scan rates, (d) charge–discharge GITT profiles at 0.1 A g^{-1} and the corresponding diffusion coefficient values, and (e) real impedance (Z') *vs.* reciprocal square root of frequency ($\omega^{-1/2}$) plot in the low-frequency region.

4. Conclusion

In summary, we have synthesized crystal water-intercalated MoS_2 nanosheets using a facile, cost-effective, eco-friendly hydrothermal synthesis method. Morphological characterization such as FESEM and TEM shows the 2D sheet-like morphology of MoS_2 with an average thickness of 15.2 nm. HRTEM and XRD results reveal the interlayer spacing of MoS_2 to be 0.79 nm. EDX and EELS confirm the presence of Mo, S and O as constituent elements in the sample. The presence of crystal water in MoS_2 is confirmed by analysing TGA, XPS, and FTIR spectra. Benefitting from its enlarged interlayer spacing and interlayer water content, the as-synthesized MoS_2 demonstrated good electrochemical performance as a cathode material in ZIBs. The material offered a high specific discharge capacity of 197 mA h g^{-1} at 0.1 A g^{-1} and a good rate performance too. A detailed electrochemical kinetic analysis revealed the diffusion-dominated charge storage reactions with Zn^{2+} diffusion coefficients of 10^{-10} to 10^{-13} cm^2 s^{-1}. This study will further widen the scope of crystal water intercalation-based layered materials for high-performance energy storage applications.

Author contributions

Muruganandham Hariram: conceptualization, investigation, data curation, methodology and writing – original draft. Manoj Kumar: resources, investigation and supervision. Kamlendra Awasthi: resources, investigation and supervision. Debasish Sarkar: conceptualization, funding acquisition, investigation, methodology, formal analysis, project administration, resources, supervision and writing – review and editing. Prashanth W. Menezes: supervision, formal analysis and writing – review and editing.

Conflicts of interest

The authors declare no competing interests.

Acknowledgements

M. H. gratefully acknowledges UGC-DAE CSR Indore for the research fellowship. D. S. acknowledges financial support from ISRO-RAC-S MNIT Jaipur through project RAC-S/PRO/21-22/02 and UGC-DAE CSR Indore through project CRS/2021-22/01/442. MRC, MNIT Jaipur is also gratefully acknowledged for providing different characterization facilities. P. W. M. acknowledges funding by the German Federal Ministry of Education and Research in the framework of the project Catlab (03EW0015A/B).

References

1 Y. Tian, G. Zeng, A. Rutt, T. Shi, H. Kim, J. Wang, J. Koettgen, Y. Sun, B. Ouyang, T. Chen, Z. Lun, Z. Rong, K. Persson and G. Ceder, *Chem. Rev.*, 2021, **121**, 1623–1669.

2 T. Zhang, Y. Tang, S. Guo, X. Cao, A. Pan, G. Fang, J. Zhou and S. Liang, *Energy Environ. Sci.*, 2020, **13**, 4625–4665.
3 N. Zhang, X. Chen, M. Yu, Z. Niu, F. Cheng and J. Chen, *Chem. Soc. Rev.*, 2020, **49**, 4203–4219.
4 W. S. V. Lee, T. Xiong, X. Wang and J. Xue, *Small Methods*, 2021, **5**, 2000815.
5 T. Stephenson, Z. Li, B. Olsen and D. Mitlin, *Energy Environ. Sci.*, 2014, **7**, 209–231.
6 W. Wang, C. Li, S. Liu, J. Zhang, D. Zhang, J. Du, Q. Zhang and Y. Yao, *Adv. Energy Mater.*, 2023, **13**, 2300250.
7 W. Liu, J. Hao, C. Xu, J. Mou, L. Dong, F. Jiang, Z. Kang, J. Wu, B. Jiang and F. Kang, *Chem. Commun.*, 2017, **53**, 6872–6874.
8 D. Sarkar, D. Das, S. Das, A. Kumar, S. Patil, K. K. Nanda, D. D. Sarma and A. Shukla, *ACS Energy Lett.*, 2019, **4**, 1602–1609.
9 Y. Xue, Q. Zhang, W. Wang, H. Cao, Q. Yang and L. Fu, *Adv. Energy Mater.*, 2017, **7**, 1602684.
10 P. Aggarwal, D. Sarkar, P. W. Menezes and K. Awasthi, *Int. J. Hydrogen Energy*, 2022, **47**, 41795–41805.
11 S. Li, Y. Liu, X. Zhao, K. Cui, Q. Shen, P. Li, X. Qu and L. Jiao, *Angew. Chem., Int. Ed.*, 2021, **60**, 20286–20293.
12 F. Liu, L. Li, S. Xu, J. Guo, Y. Ling, Y. Zhang, W. Gong, L. Wei, C. Wang, Q. Zhang and Q. Li, *Energy Storage Mater.*, 2023, **55**, 1–11.
13 Z. Yao, W. Zhang, X. Ren, Y. Yin, Y. Zhao, Z. Ren, Y. Sun, Q. Lei, J. Wang, L. Wang, T. Ji, P. Huai, W. Wen, X. Li, D. Zhu and R. Tai, *ACS Nano*, 2022, **16**, 12095–12106.
14 L. Liu, W. Yang, H. Chen, X. Chen, K. Zhang, Q. Zeng, S. Lei, J. Huang, S. Li and S. Peng, *Electrochim. Acta*, 2022, **410**, 140016.
15 F. Niu, Z. Bai, Y. Mao, S. Zhang, H. Yan, X. Xu, J. Chen and N. Wang, *Chem. Eng. J.*, 2023, **453**, 139933.
16 K. D. Rasamani, F. Alimohammadi and Y. Sun, *Mater. Today*, 2017, **20**, 83–91.
17 S. Li, Y. Liu, X. Zhao, Q. Shen, W. Zhao, Q. Tan, N. Zhang, P. Li, L. Jiao and X. Qu, *Adv. Mater.*, 2021, **33**, 2007480.
18 F. Ming, H. Liang, Y. Lei, S. Kandambeth, M. Eddaoudi and H. N. Alshareef, *ACS Energy Lett.*, 2018, **3**, 2602–2609.
19 H. Li, Q. Yang, F. Mo, G. Liang, Z. Liu, Z. Tang, L. Ma, J. Liu, Z. Shi and C. Zhi, *Energy Storage Mater.*, 2019, **19**, 94–101.
20 H. Liang, Z. Cao, F. Ming, W. Zhang, D. H. Anjum, Y. Cui, L. Cavallo and H. N. Alshareef, *Nano Lett.*, 2019, **19**, 3199–3206.
21 H. Zhang, W. Wu, Q. Liu, F. Yang, X. Shi, X. Liu, M. Yu and X. Lu, *Angew. Chem., Int. Ed.*, 2021, **60**, 896–903.
22 K. C. Lalithambika, K. Shanmugapriya and S. Sriram, *Appl. Phys. A*, 2019, **125**, 817.
23 A. T. Massey, R. Gusain, S. Kumari and O. P. Khatri, *Ind. Eng. Chem. Res.*, 2016, **55**, 7124–7131.
24 H. Liu, J.-G. Wang, W. Hua, Z. You, Z. Hou, J. Yang, C. Wei and F. Kang, *Energy Storage Mater.*, 2021, **35**, 731–738.
25 K. S. W. Sing, *Pure Appl. Chem.*, 1985, **57**, 603–619.
26 J. Yang, L. Lian, H. Ruan, F. Xie and M. Wei, *Electrochim. Acta*, 2014, **136**, 189–194.
27 Z. Sheng, P. Qi, Y. Lu, G. Liu, M. Chen, X. Gan, Y. Qin, K. Hao and Y. Tang, *ACS Appl. Mater. Interfaces*, 2021, **13**, 34495–34506.
28 H. K. Rathore, M. Hariram, M. K. Ganesha, A. K. Singh, D. Das, M. Kumar, K. Awasthi and D. Sarkar, *J. Colloid Interface Sci.*, 2022, **621**, 110–118.
29 H. K. Rathore, M. Hariram, M. K. Ganesha, A. K. Singh, D. Das, M. Kumar, K. Awasthi and D. Sarkar, *Sustainable Energy Fuels*, 2023, **7**, 2613–2626.
30 D. W. Dees, S. Kawauchi, D. P. Abraham and J. Prakash, *J. Power Sources*, 2009, **189**, 263–268.
31 F. Shao, Y. Huang, X. Wang, Z. Li, X. Huang, W. Huang, L. Dong, F. Kang, W. Liu and C. Xu, *Chem. Eng. J.*, 2022, **448**, 137688.
32 C. Li, C. Liu, Y. Wang, Y. Lu, L. Zhu and T. Sun, *Energy Storage Mater.*, 2022, **49**, 144–152.
33 J. Lai, H. Zhu, X. Zhu, H. Koritala and Y. Wang, *ACS Appl. Energy Mater.*, 2019, **2**, 1988–1996.
34 C. W. Kang, J. Park, G. H. Kim, K. C. Ko and S. U. Son, *ACS Appl. Mater. Interfaces*, 2023, **15**, 7887–7898.
35 P. Cao, N. Chen, W. Tang, Y. Liu, Y. Xia, Z. Wu, F. Li, Y. Liu and A. Sun, *J. Alloys Compd.*, 2022, **898**, 162854.